Design solutes to achieve columnar-to-equiaxed transition and grain refinement in cast multi-principal-element alloys

X.W. Liu[a,*], N. Gao[a], Z.H. Yin[a], Y.S. Wang[a], J.Q. Yao[a], Z.T. Fan[a], Y. Yang[b,*]

[a] State Key Laboratory of Materials Processing and Die & Mould Technology, Huazhong University of Science and Technology, Wuhan 430074, China

[b] Oak Ridge National Laboratory, Materials Science and Technology Division, Oak Ridge, TN 37831, USA

*Corresponding authors: liuxw@hust.edu.cn (X.W. Liu), yangying@ornl.gov (Y. Yang)

Abstract:

The multi-principal-element alloys (MPEAs), also referred to as high-entropy alloys (HEAs) have attracted extensive attention during the last decade and a half due to their unique and excellent properties. However, many MPEAs show coarse and anisotropic columnar grains in the as-cast state. While constitutional supercooling (CS)-driven parameters have been widely used to evaluate and predict the effect of solutes on columnar-to-equiaxed transition (CET) and grain refinement of diluted binary alloys, similar studies are lacking on MPEAs. Due to the multiple solute elements (solutes) and their high concentrations, the CS-driven parameters for MPEAs are different from those proposed for diluted binary alloys. Here, we derived the CS-driven parameters, including undercooling parameter and growth restriction factor, for MPEAs based on their physical significances, with the help of calculated phase diagrams. The calculated CS-driven

parameters were then used to predict the effect of a solute on CET and grain refinement in NiCoFeCr MPEAs. Additional alloying solutes Nb, Ti and V in the NiCoFeCr MPEA were also evaluated for their different CS-driven characteristics. The grain size of the as-solidified microstructures of NiCoFeCr with and without Nb, Ti, and V were compared and interpreted with the predicted tendency of the CS-driven parameters.

Keywords: Multi-principal-element alloy; High-entropy alloy; Solidification, Columnar-to-equiaxed transition, Grain refinement; Solute segregation; Constitutional supercooling

1. Introduction

Single-phase multi-principal-element alloys (MPEAs) have attracted extensive attention due to their unique properties (e.g., [1-22].). From a thermodynamical point of view, these alloys have much higher configurational mixing entropies than most of the single-principal-element conventional alloys, which was the reason for the definition of "high-entropy alloy (HEA)" by Yeh et al. [2]. MPEAs, because of their composition characteristics, result in the absence of "solvent" and "solute" atoms and a breakdown of the textbook concept of solute-involved behaviors, e.g., the solidification process that is closely correlated with the solute behaviors. In particular, the constitutional supercooling (CS) caused by partitioning solutes into the front of the solid-liquid interface remains unclear due to the complex compositions of the MPEAs. CS has been recognized as an important factor in enabling the formation, and refining, of equiaxed grain structures [23]. Several CS-driven parameters linking to grain growth, such as constitutional supercooling (designated as P) and growth restriction factor (GRF, designated as Q), have been proposed and proved to be effective for the grain growth prediction in traditional dilute solid solutions [23-27]. Both parameters tend to increase with the increasing solute concentrations, which contributes to stronger grain refinement [28]. However, this is not always expected in MPEAs where the concentrations for individual elements are much higher than those of solutes in traditional alloys. For example, the mostly investigated NiCoFeCrMn HEA, first proposed by Cantor et al. [1], and its subsets of NiCoFeCr and NiCoCr medium-entropy alloys (MEAs), exhibited coarse columnar grains in the as-cast

state [29-31]. The coarse grains in the as-cast microstructures of these MPEAs raised a question whether the CS-driven parameters are applicable to MPEA systems. However, fundamental research to answer these scientific questions are still lacking, let alone the composition design strategies for grain refinement of the MPEAs.

Understanding the solute effect on grain refinement of MPEAs is of practical importance. Fine-grained microstructures are generally required for cast alloys/ingots to meet the mechanical/ corrosion resistant properties or prevent the deformation tearing and cracking in the following thermomechanical treatments. For example, for Al alloys, a fine grain size (< 200 μm) is used to indicate that a casting or an ingot is of high quality [32]. A fine grain size also correlates with homogeneous microstructure, compared with the anisotropic columnar grains. Although there are a number of methods that have been proved to refine effectively the as-cast microstructures, such as inoculation, rapid solidification, melt stirring, etc. (e.g. [25, 33-35]), the solute elements is the most crucial consideration in grain refinement of MPEAs due to the following reasons. First, utilizing solute effect (i.e., adding proper alloying element) is an effective approach for significant columnar-to-equiaxed transition (CET) and grain refinement [24, 36-39]. Second, the solute behaviors are essential factors to ensure the effective exerting of other methods of grain refinement. For instance, in some Al alloys with low solute contents, although there are adequate powerful grain refiners (e.g. TiB_2 and Al_3Ti particles), specific solute elements (e.g. Ti) and adequate concentrations are still required to provide a sufficient CS to compensate a certain degree of undercooling to reach the critical nucleation

undercooling, where further nucleation can occur on particles present in the constitutionally undercooled regions [24, 40]. This also occurs in Mg alloys [41]. For adopting the melt stirring by external fields to achieve grain refinement, the solute effect also plays a key role in both inducing dendrite necking and further fusing to fragments, and increasing the extent of the undercooled zone and thus the chance of fragment survival [42]. Third, solute effect has a prevalent applicability for various kinds of casting processes of MPEAs. Some of the abovementioned grain-refining methods are difficult to implement in the generally used laboratory-scale processes, which typically involve induction/arc melting and drop/suction casting in an enclosed vacuum furnace. In these cases, using solute effect is highly practicable. To conclude, developing CS-driven parameters of solute effect suitable for MPEAs and further the solute selection strategy for CET and grain refinement based on them is of critical importance.

To address the aforementioned questions, here we derive the CS-driven parameters for MPEAs based on their physical significance and further we chose the NiCoFeCr MPEA as the base alloy to validate the prediction. Finally, we present solute selection strategy based on the established parameters for grain refinement in the NiCoFeCr MPEA. This paper is organized as the follows: The models of CS-driven parameters is described and developed for MPEAs in Section 2. The employed CALPHAD calculation and experimental methods are introduced in Section 3. The correlation between the grain features and CS-driven parameters in the NiCoFeCr MPEA system are presented in Section 4. Also, based on the established CS-driven parameters, various (NiCoFeCr)-x at.

93 pct B alloys (B is Nb, Ti, or V as the fifth alloying element) were screened
94 experimentally for grain refinement. We then compare and discuss the experimental and
95 theoretical results in Section 5.

96 **2. Constitutional supercooling related parameters**

97 *2.1 CS-driven parameters for binary systems*

98 The role of solute in controlling grain growth is related to its effect on generating
99 constitutional supercooling. The CS concept, especially its formula based on binary
100 alloys has been considered as a major milestone in the development of quantitative
101 understanding of solidification science. According to the CS-driven nucleation
102 mechanism, nucleation will occur when the amount of CS reaches the critical
103 undercooling required for nucleation. In the early 1970s, Tarshisv et al. [43] developed
104 the CS parameter (P):

105 $$P = \frac{m_L C_0 (1-k)}{k} \quad (1),$$

106 Where m_L is the slope of the liquidus, C_0 is the initial solute concentration, and k is
107 the partitioning coefficient. Both k and m_L are taken from the equilibrium binary phase
108 diagram. Increasing the solute content or/and decreasing the partitioning coefficient (i.e.
109 stronger segregant) could produce a higher P value (here only the case of k<1 is
110 discussed, unless indicated otherwise). P represents the magnitude of CS that can be
111 generated during solidification. Spittle and Sadli [44] came to a conclusion that the grain
112 size reduces as P increases from zero and fall to a plateau after comparing various solutes

in Al alloys.

Afterwards, Maxwell and Hellawell [36] proposed another parameter, Growth Restrict Factor (GRF, Q):

$$\mathrm{Q} = m_L C_0 (k - 1) \quad (2),$$

Q is proportional to the amount of CS parameter, P, with the partition coefficient of k for a particular binary system. The GRF is a measure of the growth restriction effect of a solute element on the growth of new grains as they grow into a melt. It is to quantify the segregating behavior of elements upon solidification. To illustrate these two parameters evidently, a binary ideal A-B system (herein A is the solvent and B is the solute) is shown in Fig. 1a.

Although the two parameters have some correlations, the differences between each other could be understood by their physical meanings [45]. The equilibrium liquidus temperature, T_{Le}, and the actual temperature, T_a, in the solid-liquid interface are given as:

$$T_{Le} = T_0 + m_L C_0 \quad (3),$$

$$T_a = T_0 + m_s C_s \quad (4),$$

Where, T_0 is the melting point of solvent A and m_s is the slope of solidus. Assuming that there is no thermal undercooling, the CS, ΔT_{CS}, is expressed by the difference between T_{Le} and T_a:

$$\Delta T_{CS} = T_{Le} - T_a = m_L C_0 - m_s C_s = m_L C_0 - \frac{m_L C_s}{k_0} = m_L (C_0 - C_L) \quad (5),$$

If a Scheil condition (zero diffusion of solid and instantaneous diffusion of liquid) is used, and the growth of a single grain is considered, the CS could be related to the fraction solid, f_s. By substituting the Scheil equations into equation (3) to obtain

$$\Delta T_{CS} = m_L C_0 \left(1 - \frac{1}{(1-f_s)^{1-k}}\right) \quad (6),$$

Substituting the lever rule in equilibrium solidification state, $C_L = \frac{C_0}{1-(1-k)f_s}$, into equation (4), the equation becomes:

$$\Delta T_{CS} = m_L C_0 \left(1 - \frac{1}{1-(1-k)f_s}\right) \quad (7),$$

At $f_s = 1$,

$$\Delta T_{CS} = \frac{m_L C_0 (1-k)}{k} = P \quad (8),$$

If we focus on the initial rate of development of the constitutionally supercooled zone, the initial rate is defined by $\frac{d\Delta T_{CS}}{df_s}$.

$$\frac{d\Delta T_{CS}}{df_s} = -\frac{m_L C_0 (1-k)}{(1-(1-k)f_s)^2} \quad (9),$$

At $f_s = 0$,

$$\frac{d\Delta T_{CS}}{df_s} = m_L C_0 (k-1) = Q \quad (10),$$

The same formulas could be obtained by using either lever rule or Scheil equation. Readers are referred to the previous works for details [45-49]. In binary phase diagrams (Fig. 1a) with straight lines, the values of P and Q mathematically equal to the differences between the liquidus and solidus at the composition of C_0 and kC_0, respectively [47]. The

CS parameter P is the maximum value of ΔT_{cs} that is possible. This could be seen from equation (3) in which the maximum value of ΔT_{cs} is obtained when C_L reaches its maximum, i.e. C_0/k. This point of composition is corresponding to the ending moment of solidification ($f_s = 1$). The GRF, however, is denoted as initial rate of development of supercooling with respect to fraction solid, i.e. corresponding to $f_s = 0$. It is considered as the magnitude of how rapidly the CS zone is built up at the starting point of solidification. In this case, the equilibrium content of solid is kC_0 (actually the solid is just ready to form at this time). In general, high Q value requires high m_L (absolute value), low k and high C_0, which leads to a more rapid achievement of the maximum.

2.2 CS-driven parameters in multi-principal-element alloys

Both CS-driven parameters have been used in binary alloys for solute selection of grain refinement. Then attempts have been made to expand them to multicomponent alloys. Chai et al. [50] suggested to determine the Q value by summing those of different solutes present in a system, however, Easton and StJohn [45] indicated that summation of the individual Q values overestimates the total Q. Later, Quested and Greer [46] indicated the possibility to use thermodynamic modelling software to evaluate the partitioning coefficient and the liquidus slope to calculate the Q values in dilute ternary alloys. However, calculating Q values in MPEAs has not been reported in literature.

Here, we derive CS-driven parameters for MPEAs in terms of their definitions. We first simplify our MPEAs as pseudo-binary systems, M-B, where “M” represents the

solvent and "B" the solute element, with a schematic pseudo-binary phase diagram shown in Fig. 1b. The pseudo-binary phase diagram has been a widely applied method for MPEAs [51, 52]. Although the *M*-*B* pseudo-binary phase diagram in Fig. 1b seems analogous to that of *A*-*B* ideal binary system (Fig. 1a), a distinct difference could be clearly seen, i.e. a solidification gap for the base alloy, *M*, rather than a fixed melting point like that of the pure solvent A, is existing (defined as ΔT_{M0} marked in the plot). The solidification gap for *M* could influence the grain growth to a certain extent depending on its composition, since it is also generated by the solute redistribution and inevitably contributes to the total CS of *M*-*B* system. Therefore, the contribution of ΔT_{M0} to *P* and *Q* should be considered. Here we proposed a simple method to use the original definition to calculate both CS-driven parameters. Assuming that the solidus and liquidus are straight lines in Fig. 1b (which have been approximatively the case in numerous MPEA systems and focused concentration ranges as to be shown later), we calculated both parameters based on their definitions. The equilibrium liquidus temperature, T_{Le}, and the actual temperature, T_a, could be expressed as:

$$T_{Le} = T_L^0 + m_L C_L$$

$$T_a = T_S^0 + m_S C_S$$

Where C_L and C_S are the solute concentrations in the liquid and solid phases, respectively. At a certain temperature during solidification process, i.e. $T_{Le} = T_S$, substituting $k = C_S/C_L$ and $\Delta T_{M0} = T_L^0 - T_S^0$ into the above equations, it comes to be:

$$k = \frac{m_L C_L + \Delta T_{M0}}{m_S C_L}$$

Thus, it can be seen that k is changing with the advance of solidification in MPEAs, differing from the constant in idealized binary systems. According to the physical meaning of Q, at the beginning of solidification (i.e. $f_s = 0$), $C_L = C_0$, then the above equation is changed to be:

$$k = \frac{m_L C_0 + \Delta T_{M0}}{m_S C_0} \quad (9),$$

Substituting equation (8) to equation (2) comes out to be:

$$Q = m_L c_0 \left(\frac{m_L}{m_S} + \frac{\Delta T_{M0}}{m_S c_0} - 1\right) \quad (10),$$

According to the physical meaning of P, at $f_s = 1$, $C_S = C_0$, the equation (1) is transformed to be:

$$\mathrm{P} = m_L C_0 - m_S C_0 + \Delta T_{M0} \quad (11).$$

Eventually, both CS-driven parameters for MPEAs were established according to their initial designations. In the following sections, these parameters were adopted to study the grain growth characteristics and solute selection on the basis of a model HEA, NiCoFeCr, *via* thermodynamic calculation in association with experiments.

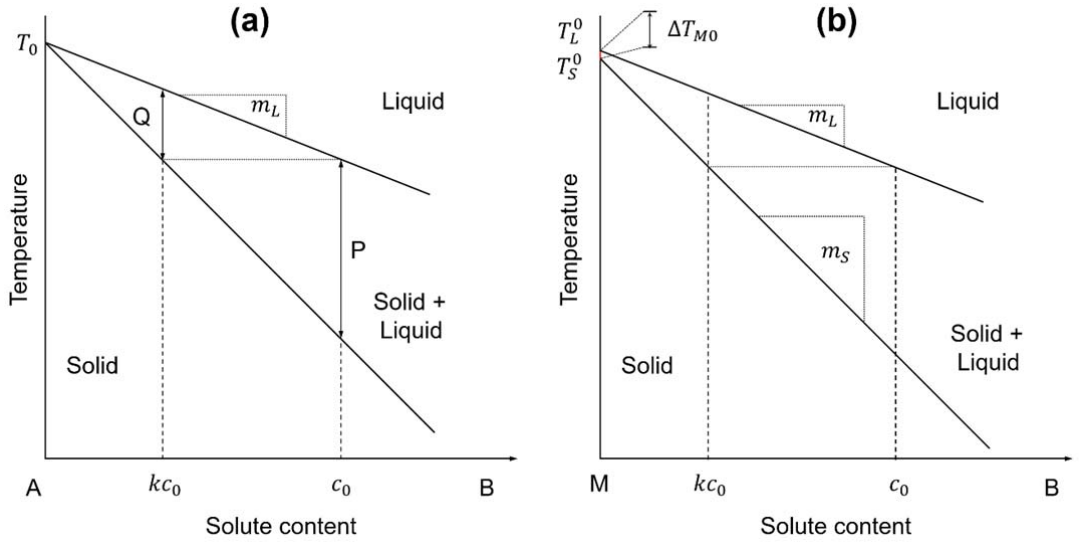

Fig. 1 Schematic phase diagrams of (a) idealized binary A-B system in A-rich portion and (b) pseudo-binary M-B system where the matrix/solvent M is a multicomponent alloy with constituent elements ≥2.

3. Calculation and experimental

3.1 Calculation

Phase diagrams were investigated by means of the CALPHAD (CALculation of PHAse Diagrams) approach using TcNi11 database and Thermo-Calc software [53]. Here both CS-driven parameters were obtained based on the calculated pseudo-binary M-B phase diagrams. With the (NiCoFeCr)-B systems, different "B" elements were evaluated to elucidate their effect on the grain growth features. Some common grain refining elements including Nb, Al, Ti, Ta, C, V, Cu, Mn and Mo were selected for investigation. The parameters (m_S, m_L and ΔT_{M0}) were obtained from the pseudo-binary phase diagrams to determine the two CS-driven parameters. Solidification simulation follows

the Scheil model in multicomponent systems [Chen, Shuang-Lin, Ying Yang, Sinn-Wen Chen, Xiong-Gang Lu, and Y. Austin Chang. "Solidification simulation using Scheil model in multicomponent systems." Journal of phase equilibria and diffusion 30, no. 5 (2009): 429-434.]

3.2 Experimental

To verify the as-cast microstructures, the relevant alloys were made and their microstructures were observed. The alloys were prepared by arc melting mixtures of the pure metals (purity >99.9 wt. pct) in a high-purity argon atmosphere. The arc melting chamber containing the raw materials was evacuated to ~5×10^{-2} Pa, flushed twice with pure Ar with pump downs in between, and finally backfilled with Ar to a pressure of ~5×10^{4} Pa. Then, a small piece of pure Ti was melted to getter any residual oxygen before the alloys were melted. The buttons were flipped and remelted five times to ensure chemical homogeneity before drop-casting into a rectangular copper mold measuring $10 \times 17 \times 70$ mm^3.

To examine the as-solidified microstructures, the ingot cross sections were ground with SiC papers to a grit size of 7 μm and then electro-polished using Struers LectroPol-5 for 10 s in a mixture of 10 vol. pct perchloric acid and 90 vol. pct ethanol at room temperature and an applied voltage of 40 V. The microstructural characterization was measured using a Zeiss AURIGA FIB-SEM equipped with an energy dispersive X-ray spectroscopy (EDX) X-Max^N from Oxford Instruments at an accelerating voltage of 20

kV. We focused on the lower part of the cast ingots, away from the entrance of the mold, which tends to have more stable solidification conditions. Grain sizes were measured with the linear intercept method outlined in ASTM E112-10. In this work, equiaxed grains were defined as those with an aspect ratio less than 2, while those with larger aspect ratios were defined as columnar grains [54]. Flat dog-bone shaped tensile specimens with a gauge length of 20 mm were machined from the cast ingots by electric discharge machining with their longitudinal axes parallel to the mold-filling direction. The tensile specimens were ground carefully on each side through 1000-grit SiC paper, resulting in a final specimen thickness of ~1.2 mm and a gauge section width of ~4 mm. The tensile tests were performed using a SHIMADZU AG-100 KN testing machine at an engineering strain rate of 10^{-3} s^{-1} in air at room temperature. At least two tests using samples from different parts of the ingots were performed for each alloy.

4. Results and discussion

4.1 Correlation between the predicted CS-driven parameters and the solidification microstructure of NiCoFeCr system

Many MEPAs show coarse grains after solidification, e.g. well-studied CrMnFeCoNi and some of its subsets, although they have highly-concentrated individual elements, which implies that the constituent elements cannot generate sufficient grain growth restriction effect. To elucidate this issue, the two CS-driven parameters for binary Ni-B, ternary NiX-B and quarternary NiXY-B subsets of the Ni-Co-Fe-Cr MPEA system (B=Co, Cr, or Fe, and X and Y are the remaining constituent elements in this system)

were calculated in terms of the equations of (9) and (10). Their dependence on the solute concentration is plotted in Fig. 2. Pure Ni, equiatomic NiX and NiXY were set as the solvent in calculating these binary, ternary and quaternary systems, respectively. The concentrations of the solutes are up to the values to reach equiatomic. The binary phase diagrams could be obtained from Ni-Cr [55], Ni-Co [56] and Ni-Fe [57], and the others were calculated by the Thermo-Calc software. The studied compositions are solidified as a single FCC phase from their phase diagrams or previous reports [30, 31], thus only the solute effect is involved with no influence from other phases. The liquidus and solidus in these systems are approximated as straight lines as treated in previous binary systems, thus there may be slight deviations from the exact values, however, the trend and their magnitude are still credible. In the Ni-B binary systems, P and Q are increased strongly with increasing Cr content, but negligibly with increasing Co content. When the solvents are equiatomic NiX or NiXY alloys, both parameters are slightly increased with Cr but unexpectedly decreased with Co. Additionally, both parameters behave similarly for most compositions but with different values. Overall, the values of both parameters are so low that a very weak grain growth restriction effect is expected.

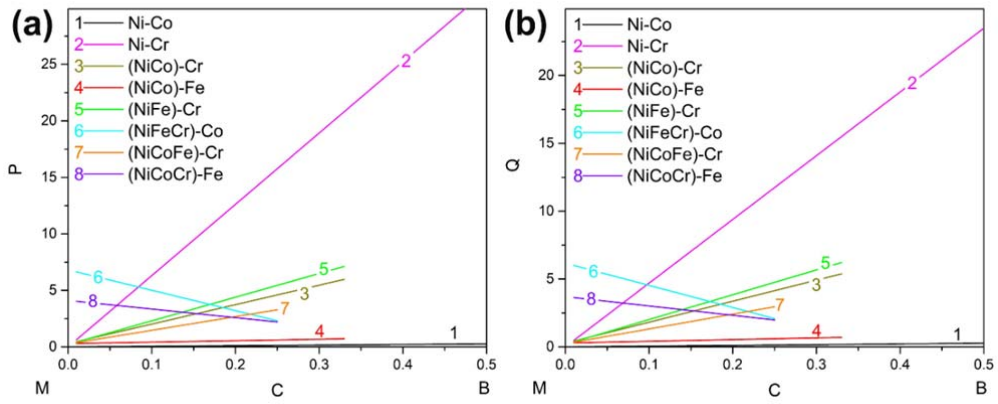

Fig. 2 Dependence of CS parameter, P (a), and growth restriction factor, Q (b), within the Ni-Co-Fe-Cr system on the solute concentration, C.

To validate the prediction, a series of equiatomic single-phase FCC alloys with gradually increased solutes, i.e. in a sequence of Ni, NiCo, NiCoFe and NiCoFeCr, were drop cast and solidified in a controlled similar condition, whose microstructures are shown in Fig. 3. The small increases in P and Q values due to adding Fe to NiCo and Cr to NiCoFe caused negligible grain refinement. Some inclusion particles are present randomly in all the studied alloys, which was common in these systems [29-31], probably coming from the raw metals and melting and casting processes. Elemental fluctuations were also observed inside the columnar grains. For example, EDS analysis in our previous work revealed Cr enrichment in the inter-dendritic area in the as-cast NiCoFeCr MPEA [30]. Even with that, the NiCoFeCr still formed columnar grain, suggesting Cr segregation is not sufficient to induce CET and grain refinement. Further analysis confirmed that the segregation of Cr is relatively weak (26.9 at. pct in interdendrites and

23.3 at. pct in dendrite arms, respectively). The coarse as-cast NiCoFeCr microstructures suggest that the types of the solutes rather than their concentrations are more important to produce fine grains. As indicated in the previous studies, the solutes with strong segregating tendency could produce strong constituent supercooling [27]. In a summary, the constituent elements in the NiCoFeCr MPEA systems were proved to be incapable of supplying sufficient grain growth restriction effect (by their low values of *P* and *Q*). To obtain significant CET and grain refinement, additional solutes with stronger segregation are required.

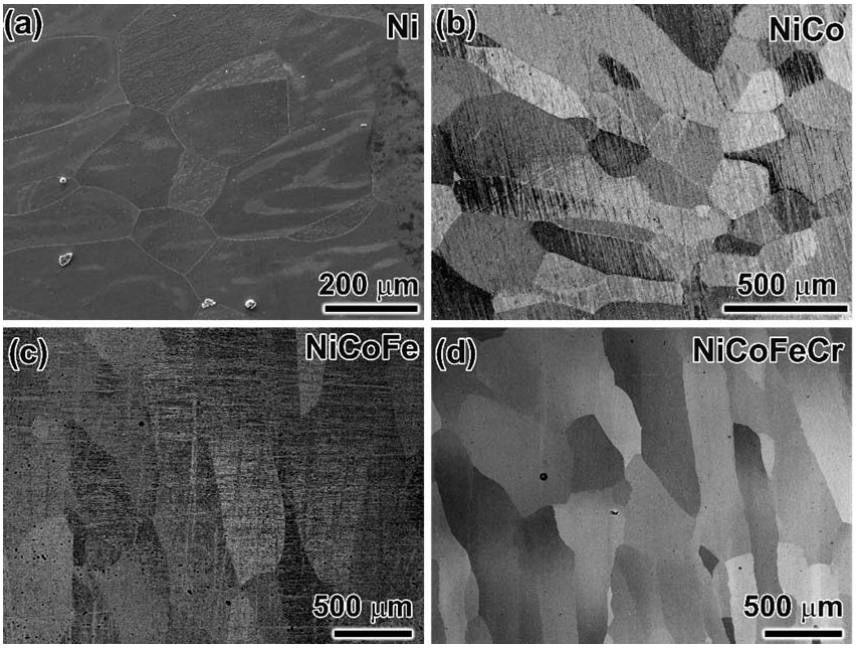

Fig. 3 Representative SEM-BSE microstructures of the as-cast equiatomic alloys: (a) Ni, (b) NiCo, (c) NiCoFe and (d) NiCoFeCr alloys.

4.2 Solute selection of NiCoFeCr MPEA for gain refinement

To identify alloying elements that have strong growth restriction effect, a high-

301 throughput screening for solute selection was conducted based on the calculation of the
302 two CS-driven parameters for MPEAs [equation (9) and (10)] with the aim to evaluate
303 their capability in achieving significant grain refinement. Nine frequently-used elements
304 (Nb, C, Cu, Mn, Mo, Al, Ta, Ti, V) were chosen and the corresponding (NiCoFeCr)-B
305 pseudo-binary phase diagrams calculated by Thermo-Calc are shown in Fig. 4. It shows
306 that different fifth elements result in great difference in liquidus and solidus lines.
307 Therefore, these elements are expected to produce different grain growth behaviors and
308 grain features (especially morphology and size). The values of *P* and *Q* vs. the elemental
309 concentration are plotted in Fig. 5. The maximum concentration is up to the endpoint of
310 liquidus in single-phase region, and for compositions having a wide single-phase region
311 or even forming an infinite solid solution, e.g. (NiCoFeCr)-Mn/Cu, the maximum
312 concentrations can be equiatomic. For all alloying elements investigated, both parameters
313 increase with increased concentrations. The increment rate of *P* is in the decreasing
314 sequence of C, Nb, Ta, Al, Ti, V, Cu, Mn and Mo, where the C and Nb are the largest, Ta,
315 Al and Ti are intermediate, and V, Cu, Mn and Mo show negligible values. However, the
316 case is slightly different for parameter *Q*: Nb has the greatest increasing trend, secondly
317 Al, Ti, Ta and C have the similar intermediate trend, and V, Cu, Mn and Mo still show
318 negligible values. To illustrate the evolution of both parameters more clearly, their
319 changes with various solutes at the same concentration of 5 at. pct are plotted in Fig. 6.
320 The potential grain growth restriction effect is clearly seen from the change of both CS-
321 driven parameters.

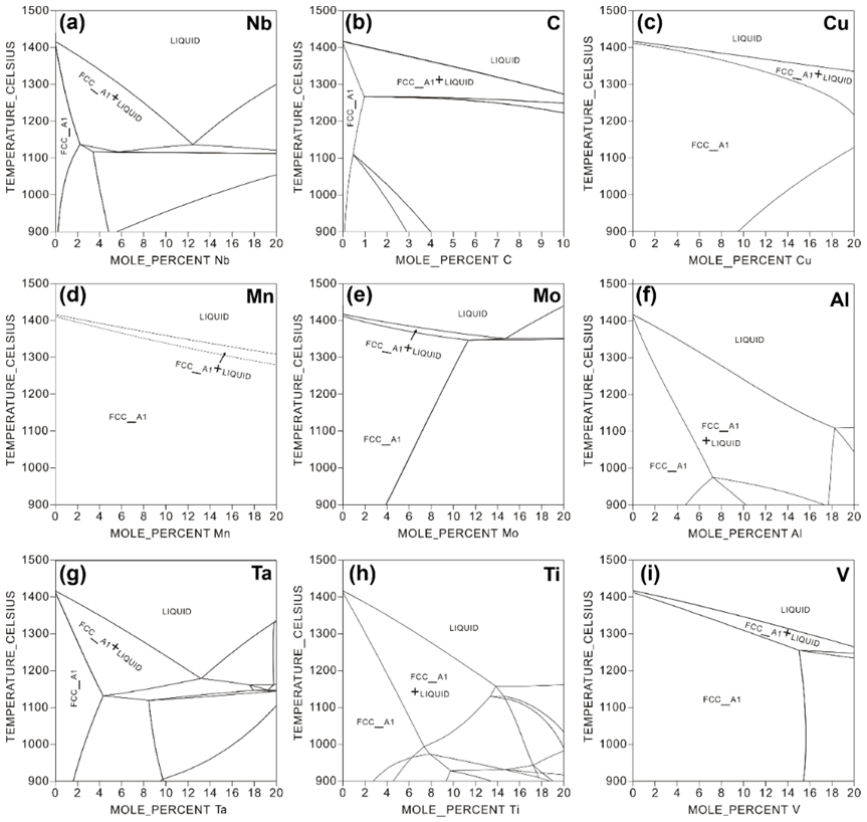

322

323 Fig. 4 The calculated pseudo-phase diagrams of (NiCoFeCr)-B systems, where B denotes

324 the selected fifth solute.

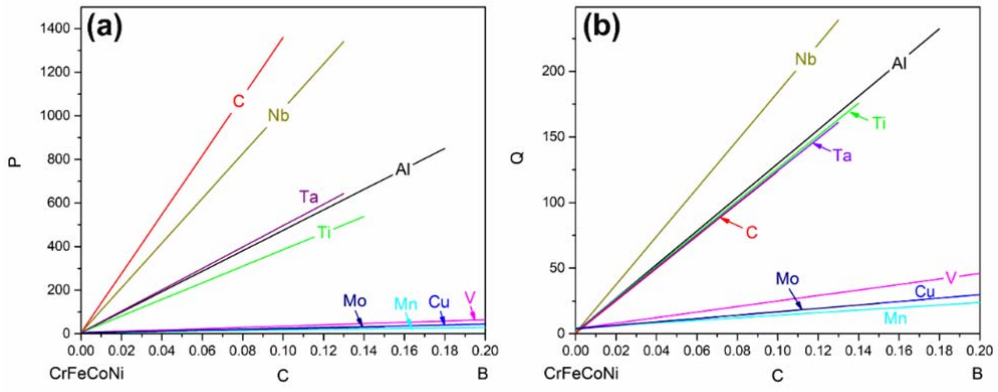

325

Fig. 5 Dependence of undercooling parameter, P (a), and growth restriction factor, Q (b), in (NiCoFeCr)-B systems on the solute (B) concentration, where B denotes the selected fifth solute.

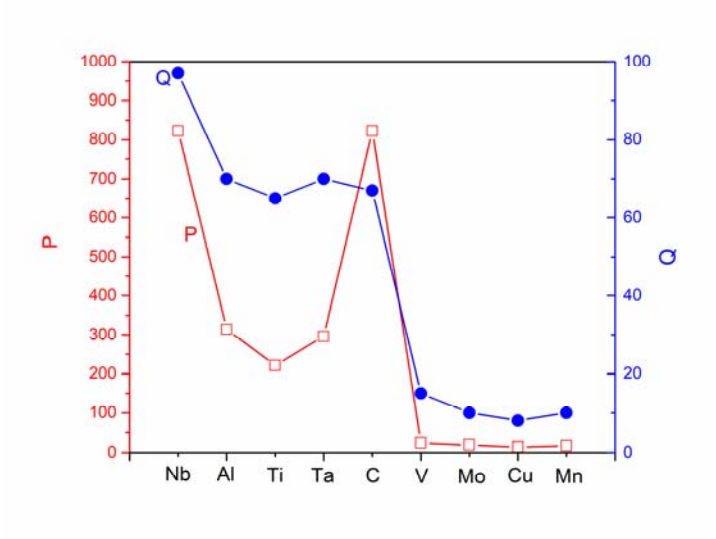

Fig. 6 The change of P and Q for (NiCoFeCr)-5 at. pct B systems, where B denotes the selected fifth solute.

Consistent with the calculated supercooling parameter P, these elements can also be categorized based on the solubility of solute in the FCC phase: Nb and C with the most limited solubility corresponding to the highest P, Al, Ta and Ti with the intermediate solubility corresponding to the intermediate P, and Cu, Mn, V and Mo with the most extensive solubility corresponding the negligible P. To see how elements from each of this category affect the grain refinement, Nb, Ti and V elements were selected to inspect their microstructures by experiments. The representative SEM-BSE images of the as-cast microstructures of (NiCoFeCr)-5 at. pct Nb, (NiCoFeCr)-5 at. pct Ti, and (NiCoFeCr)-5

at. pct V MPEAs are shown in Fig. 7. In this section, microstructures were examined near the center of the cast ingot, where the solidification conditions were controlled to be very similar for each sample. The (NiCoFeCr)-5 at. pct Ti and (NiCoFeCr)-5 at. pct Nb MPEAs exhibit a shape transition from columnar to equiaxed grains, which is in contrast with the base NiCoFeCr MPEA (Fig. 3c) which exhibits anisotropic columnar grains with average lengths of >1000 μm and widths of >100 μm. On the other hand, the V-alloyed NiCoFeCr MPEA still shows coarse columnar grains comparable to that of the NiCoFeCr base alloy, consistent with the negligible effect of V on CET and grain refinement as a result of the predicted small P and Q parameters. The Nb addition showed stronger grain refinement than the Ti addition, while this is consistent with the predicted larger P and Q value of Nb than Ti, it can also be contributed by the smaller solubility of Nb in FCC structure, which led to the formation of a large volume fraction of inter-dendritic Nb rich intermetallic phases.

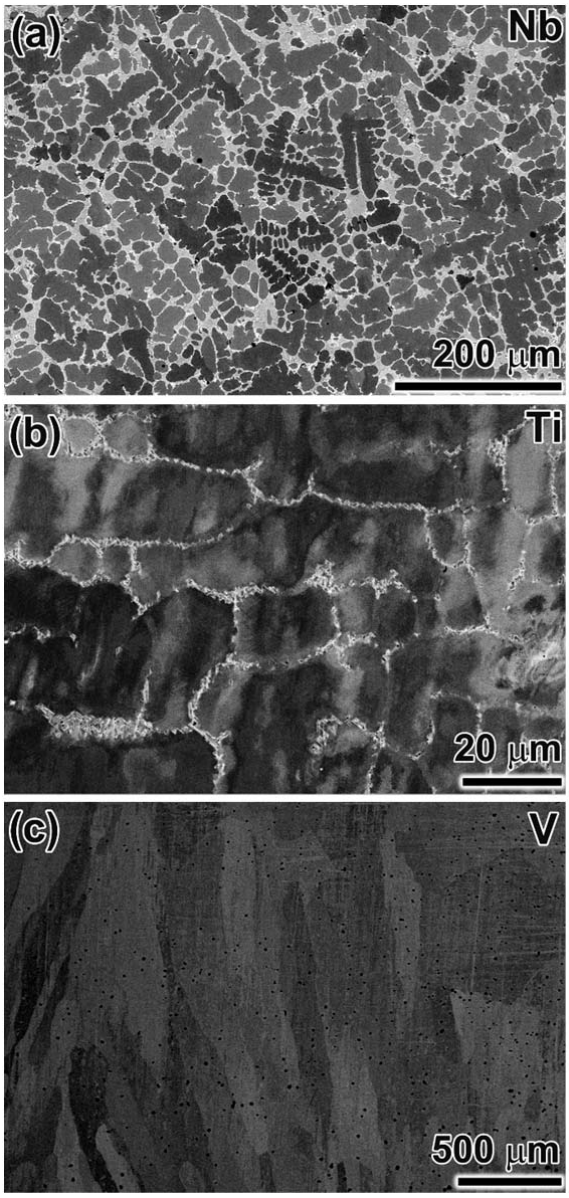

Fig. 7 SEM-BSE images of the as-cast microstructures of the (NiCoFeCr)-5 at. pct B MPEAs, where B denotes Nb, Ti and V, respectively.

4.3 Discussion

The widely studied MPEA systems, e.g. NiCoCr, NiCoFeCr, CrMnFeCoNi MPEAs, form typical coarse columnar grains after solidification. This is primarily because the

359 elements in these MPEAs have large mutual solid solubilities in favor of forming solid
360 solutions which also correlate with low P and Q and therefore do not segregate strongly.
361 Therefore, solutes with strong CS-driven parameters (P and Q) are needed to produce
362 strong enough constitutional supercooling and growth restriction effect for grain
363 refinement. However, solutes with strong CS-driven parameters also promote the
364 nucleation of solute-rich intermetallic or second phases in the inter-dendritic area during
365 solidification.

366 Fig. 8a shows the calculated solidification pathways of (NiCoFeCr)-5 at. pct Nb,
367 (NiCoFeCr)-5 at. pct Ti and (NiCoFeCr)-5 at. pct V MPEAs. It shows that at the final
368 stage of solidification, there are Nb rich laves, Ti rich laves and V rich BCC phases
369 formed in the inter-dendritic areas of 5Nb-, 5Ti- and 5V-containing NiCoFeCr MPEAs,
370 respectively. The mole fraction of the inter-dendritic intermetallic phases is the largest for
371 Nb, and least for V. This trend is consistent with the solubility of each element in FCC in
372 Fig. 4 with Nb being the smallest and V the largest. The phase fractions observed in the
373 experimental micrographs are in a qualitative agreement with the calculated results. In
374 Fig. 8b, the composition of Nb, Ti and V in liquid *vs.* the mole fraction of liquid is
375 plotted. Only the portion of liquid corresponding to the primary solidification FCC phase
376 was plotted in Fig. 8b. This plot shows that with solidification progressing, i.e., the mole
377 fraction of liquid decreases, and the content of Nb, Ti and V in the liquid all increased
378 with Ti increasing the most and Nb the least. The saturation composition of Nb, Ti and V
379 in liquid corresponds to the formation of Nb rich and Ti rich Laves, and V-rich BCC

phases from liquid, respectively. The saturation of V in liquid is ~10 at. pct, which leads to negligible P and Q values as show in Fig. 4, therefore negligible grain refinement effect. It seems that Nb follows the similar trend to Ti, but its saturation composition is much lower than Ti. Combined Fig. 8b with Fig. 5, we find the saturation of 14.5 at. pct Ti in liquid corresponds to P values of 600 and Q values of 180, respectively, and 9.5 at. pct Nb corresponds to P values of 900 and Q values of 175, respectively. The almost identical Q values in the Nb and Ti cases suggest the nucleation of laves phases in both alloys requires comparable CS. To reach the same level of growth restriction, it needs a higher concentration of Ti in liquid (14.5 at. pct) than that of Nb in liquid (9.5 at. pct). In other words, for the same atomic percent of bulk alloying addition of Nb and Ti, because the calculated P and Q parameters by Nb are higher than those by Ti, the stronger grain refinement in the Nb-doping alloy than the Ti-doping one is expected.

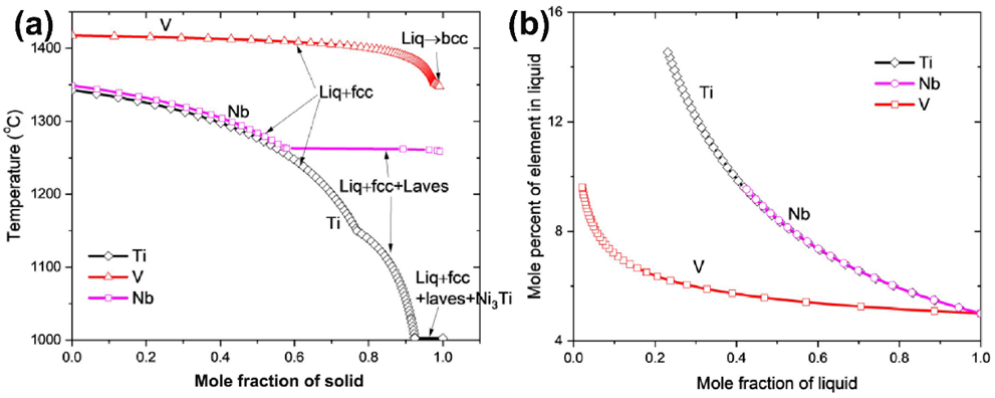

393 Fig. 8 Solidification pathways and composition evolution in 5Nb-, 5Ti- and 5V-
394 containing NiCoFeCr MPEAs. (a) Dependence of mole fraction of solid on temperature
395 showing the evolution of each phase during solidification and (b) change of solute
396 concentration with the mole fraction of liquid.

397 In both MPEAs with 5 at. pct of Nb and Ti, in addition to pronounced P and Q
398 values, the grain refinement may be also linked with the formation of intermetallic phases
399 in the inter-dendritic regions. In order to see effect of the alloying element addition on
400 grain refinement without forming such extensive intermetallic phases, a NiCoFeCr
401 MPEA was made with 2.5 at. pct addition of Ti. The SEM image and EDX mapping of
402 the 2.5 at. pct Ti MPEA were compared with the 5 at. pct Ti MPEA in Fig. 9. It shows
403 that the inter-dendritic solids in the 2.5 at. pct Ti MPEA is much less than that in the 5 at.
404 pct Ti alloy. This is consistent with the calculated solidification path of the 2.5 at. pct Ti
405 alloy as shown in Fig. 10a, where the mole fraction of inter-dendritic solids is ~3 pct,
406 much less than that (~25 pct) in the 5 at. pct Ti alloy. Fig. 10b shows the saturation
407 concentration of Ti in the 2.5 at. pct Ti alloy is ~22 at. pct, corresponding to a Q value of
408 ~275, which is much larger than that (~180) in the 5 at. pct Ti alloy, leading to stronger
409 CS-driven grain refinement in 2.5 at. pct Ti alloy. The extra Ti in the 5 at. pct Ti alloy is
410 mainly used for forming inter-dendritic Ti intermetallic phase. The combination of CS
411 effect and inter-dendritic intermetallic phases in the 5 at. pct Ti alloy resulted in a grain
412 size about twice as large as that in the 2.5 at. pct Ti alloy where the CS effect is dominant.
413 2.5 at. pct Ti and 5 at. pct Ti alloys show significant grain refinement compared to the

414 grain size of the NiCoFeCr MPEA alloy without Ti, suggesting that despite the formation
415 of intermetallic phases at inter-dendritic region plays a role in grain refinement, the
416 constitutional supercooling (P) and growth restrict factor (Q) are dominant factors in
417 refining grains.

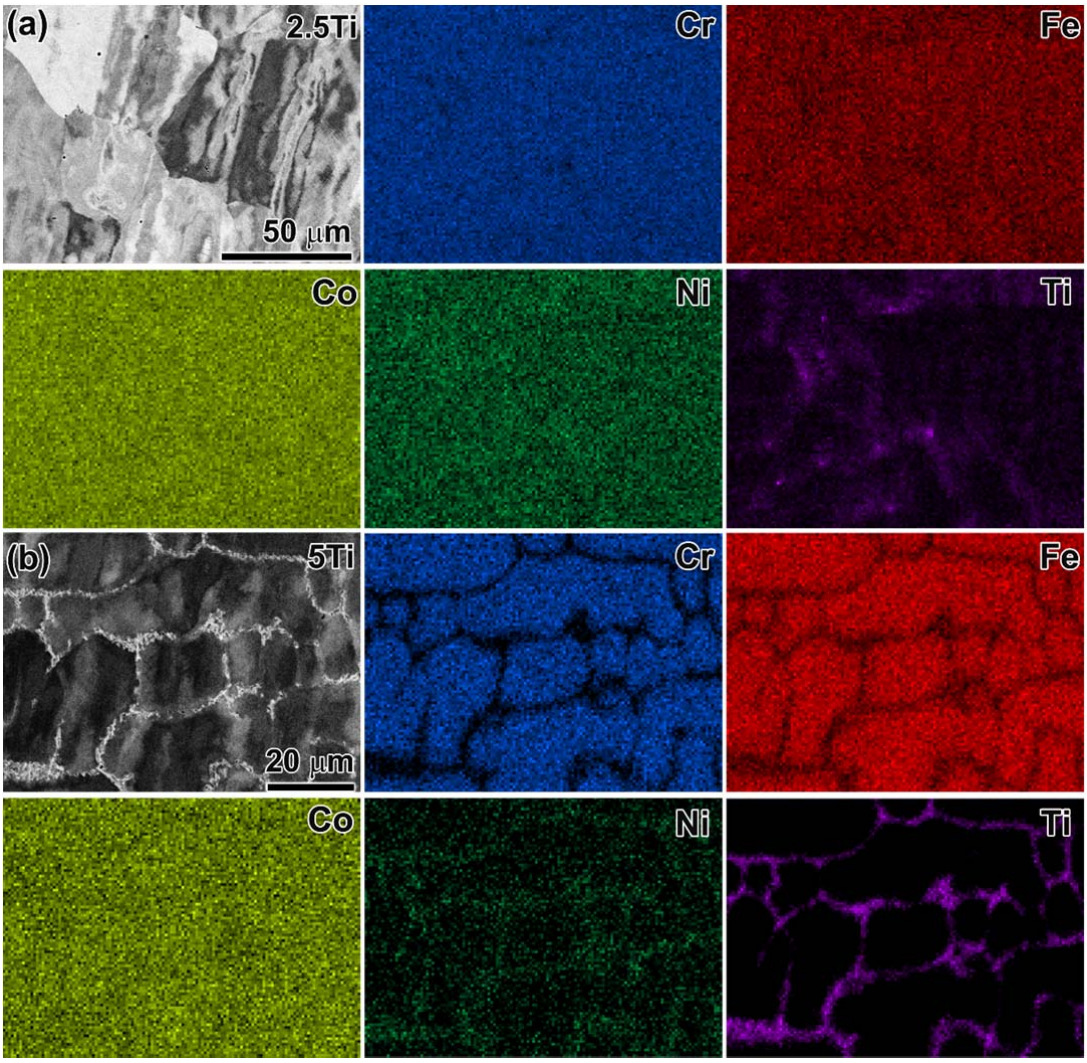

418

Fig. 9 SEM-BSE images and corresponding EDX maps of the as-cast (NiCoFeCr)-2.5 at. pct Ti (a) and (NiCoFeCr)-5 at. pct Ti (b) MPEAs.

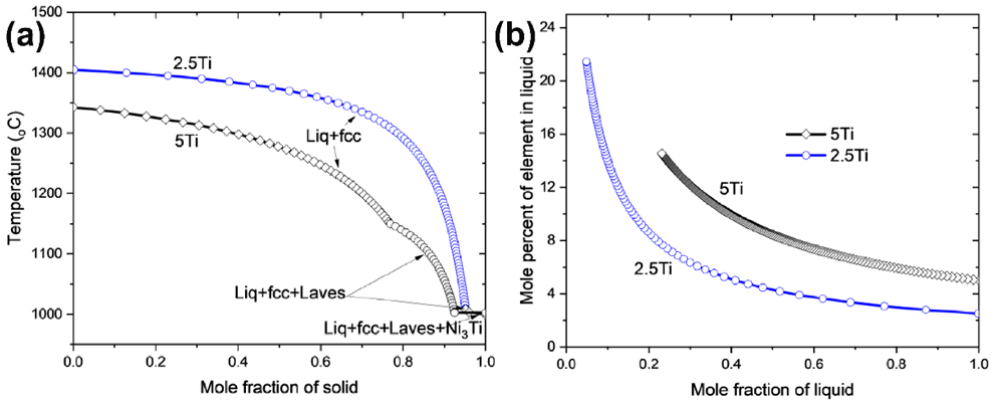

Fig. 10 Solidification pathways and composition evolution in 2.5Ti- and 5Ti-containing NiCoFeCr MPEAs. (a) Dependence of mole fraction of solid on temperature showing the evolution of each phase during solidification and (b) change of solute concentration with the mole fraction of liquid.

5. Conclusions

(1) The CS parameter (P) and growth restriction factor (Q), for multi-principal-element alloys (MPEAs) have been derived by taking into account of their physical significance. The two CS-driven parameters were described by:

$$\mathrm{P} = m_L C_0 - m_S C_0 + \Delta T_{M0}$$

$$Q = m_L c_0 \left(\frac{m_L}{m_S} + \frac{\Delta T_{M0}}{m_S c_0} - 1 \right)$$

(2) The two CS-driven parameters can be calculated readily by pseudo-binary diagrams for numerous systems with the liquidus and solidus being approximated by straight lines or calculated by thermodynamic solidification models for complex phase

diagrams.

(3) The two CS-driven parameters are able to explain qualitatively the effects of columnar to equiaxed transition and grain refinement induced by an alloyed element to an MPEA. Taking the typical NiCoFeCr alloy as an example, the parameters show that each constituent element have very weak effect on growth restriction albeit with a high concentration.

(4) Nine other systems NiCoFeCr-B (B=Nb, Al, Ti, Ta, C, V, Cu, Mn and Mo) were evaluated with the aid of thermodynamic calculation and their P and Q values inversely correlates with the solubility of each B element in the FCC structure. Experimental study on Nb addition resulted in the largest grain refinement, Ti intermediate and V negligible, which corresponds well with the predicted P and Q values.

(5) Through the comparison of 2.5 at. pct Ti and 5 at. pct Ti alloying additions on grain refinement, this work suggests that despite the formation of intermetallic phases at inter-dendritic region plays a role in grain refinement, the constitutional supercooling and growth restrict factor are dominant factors in refining grains.

Acknowledgements

Research sponsored by the National Natural Science Foundation of China (51971099), X.W.L., and the U.S. Department of Energy, Office of Science, Basic Energy Sciences, Materials Sciences and Engineering Division, Y.Y.

Declaration of Competing Interest

The authors declare no financial and personal relationships with other people or organizations that can inappropriately influence our work, there is no professional or other personal interest of any nature or kind in any product, service and/or company that could be construed as influencing the position presented in, or the review of, the manuscript submitted.

References

[1] B. Cantor, I.T.H. Chang, P. Knight, A.J.B. Vincent, Microstructural development in equiatomic multicomponent alloys, Mater. Sci. Eng. A 375-377 (2004) 213-218, https://doi.org/10.1016/j.msea.2003.10.257.

[2] J.W. Yeh, S.K. Chen, S.J. Lin, J.Y. Gan, T.S. Chin, T.T. Shun, C.H. Tsau, S.Y. Chang, Nanostructured high-entropy alloys with multiple principal elements: novel alloy design concepts and outcomes, Adv. Eng. Mater. 6(5) (2004) 299-303, https://doi.org/10.1002/adem.200300567.

[3] S. Guo, C. Ng, J. Lu, C.T. Liu, Effect of valence electron concentration on stability of fcc or bcc phase in high entropy alloys, J. Appl. Phys. 109(10) (2011) 103505, https://doi.org/10.1063/1.3587228.

[4] O.N. Senkov, J.M. Scott, S.V. Senkova, D.B. Miracle, C.F. Woodward, Microstructure and room temperature properties of a high-entropy TaNbHfZrTi alloy, J. Alloys Compd. 509(20) (2011) 6043-6048, https://doi.org/10.1016/j.jallcom.2011.02.171.

[5] F. Otto, A. Dlouhý, C. Somsen, H. Bei, G. Eggeler, E.P. George, The influences of temperature and microstructure on the tensile properties of a CoCrFeMnNi high-entropy alloy, Acta Mater. 61(15) (2013) 5743-5755, https://doi.org/10.1016/j.actam at.2013.06.018.

[6] B. Gludovatz, A. Hohenwarter, D. Catoor, E.H. Chang, E.P. George, R.O. Ritchie, A fracture-resistant high-entropy alloy for cryogenic applications, Science 345 (2014) 1153-1158, https://doi.org/10.1126/science.1254581.

[7] Y. Zhang, T.T. Zuo, Z. Tang, M.C. Gao, K.A. Dahmen, P.K. Liaw, Z.P. Lu, Microstructures and properties of high-entropy alloys, Prog. Mater Sci. 61 (2014) 1-93, https://doi.org/10.1016/j.pmatsci.2013.10.001.

[8] N.N. Guo, L. Wang, L.S. Luo, X.Z. Li, Y.Q. Su, J.J. Guo, H.Z. Fu, Microstructure and mechanical properties of refractory MoNbHfZrTi high-entropy alloy, Mater. Design 81 (2015) 87-94, https://doi.org/10.1016/j.matdes.2015.05.019.

[9] N.D. Stepanov, D.G. Shaysultanov, G.A. Salishchev, M.A. Tikhonovsky, Structure and mechanical properties of a light-weight AlNbTiV high entropy alloy, Mater. Lett. 142 (2015) 153-155, https://doi.org/10.1016/j.matlet.2014.11.162.

[10] Z. Zhang, M.M. Mao, J. Wang, B. Gludovatz, Z. Zhang, S.X. Mao, E.P. George, Q. Yu, R.O. Ritchie,

Nanoscale origins of the damage tolerance of the high-entropy alloy CrMnFeCoNi, Nat Commun 6 (2015) 10143, https://doi.org/10.1038/ncomms10143.
[11] Z.P. Lu, H. Wang, M.W. Chen, I. Baker, J.W. Yeh, C.T. Liu, T.G. Nieh, An assessment on the future development of high-entropy alloys: Summary from a recent workshop, Intermetallics 66 (2015) 67-76, https://doi.org/10.1016/j.intermet.2015.06.021.
[12] Z. Wang, Y. Huang, Y. Yang, J. Wang, C.T. Liu, Atomic-size effect and solid solubility of multicomponent alloys, Scripta Mater. 94 (2015) 28-31, https://doi.org/10.1016/j.scriptam at.2014.09.010.
[13] Z. Fu, W. Chen, H. Wen, D. Zhang, Z. Chen, B. Zheng, Y. Zhou, E.J. Lavernia, Microstructure and strengthening mechanisms in an FCC structured single-phase nanocrystalline $Co_{25}Ni_{25}Fe_{25}Al_{7.5}Cu_{17.5}$ high-entropy alloy, Acta Mater. 107 (2016) 59-71, https://doi.org/10.1016/j.actam at.2016.01.050.
[14] G. Laplanche, A. Kostka, O.M. Horst, G. Eggeler, E.P. George, Microstructure evolution and critical stress for twinning in the CrMnFeCoNi high-entropy alloy, Acta Mater. 118 (2016) 152-163, https://doi.org/10.1016/j.actam at.2016.07.038.
[15] Z. Li, K.G. Pradeep, Y. Deng, D. Raabe, C.C. Tasan, Metastable high-entropy dual-phase alloys overcome the strength–ductility trade-off, Nature 534 (2016) 227–230, http://dx.doi.org/10.1038/nature17981.
[16] G. Laplanche, A. Kostka, C. Reinhart, J. Hunfeld, G. Eggeler, E.P. George, Reasons for the superior mechanical properties of medium-entropy CrCoNi compared to high-entropy CrMnFeCoNi, Acta Mater. 128 (2017) 292-303, https://doi.org/10.1016/j.actam at.2017.02.036.
[17] Y. Lu, X. Gao, L. Jiang, Z. Chen, T. Wang, J. Jie, H. Kang, Y. Zhang, S. Guo, H. Ruan, Y. Zhao, Z. Cao, T. Li, Directly cast bulk eutectic and near-eutectic high entropy alloys with balanced strength and ductility in a wide temperature range, Acta Mater. 124 (2017) 143-150, https://doi.org/10.1016/j.actam at.2016.11.016.
[18] R. Chen, G. Qin, H. Zheng, L. Wang, Y. Su, Y. Chiu, H. Ding, J. Guo, H. Fu, Composition design of high entropy alloys using the valence electron concentration to balance strength and ductility, Acta Mater. 144 (2018) 129-137, https://doi.org/10.1016/j.actam at.2017.10.058.
[19] Y.Y. Zhao, H.W. Chen, Z.P. Lu, T.G. Nieh, Thermal stability and coarsening of coherent particles in a precipitation-hardened $(NiCoFeCr)_{94}Ti_2Al_4$ high-entropy alloy, Acta Mater. 147 (2018) 184-194, https://doi.org/10.1016/j.actam at.2018.01.049.
[20] T. Yang, Y.L. Zhao, Y. Tong, Z.B. Jiao, J. Wei, J.X. Cai, X.D. Han, D. Chen, A. Hu, J.J. Kai, K. Lu, Y. Liu, C.T. Liu, Multicomponent intermetallic nanoparticles and superb mechanical behaviors of complex alloys, Science 362 (2018) 933-937, https://doi.org/10.1126/science.aas8815.
[21] M. Song, R. Zhou, J. Gu, Z. Wang, S. Ni, Y. Liu, Nitrogen induced heterogeneous structures overcome strength-ductility trade-off in an additively manufactured high-entropy alloy, Appl. Mater. Today (2019) 100498, https://doi.org/10.1016/j.apmt.2019.100498.
[22] E.P. George, D. Raabe, R.O. Ritchie, High-entropy alloys, N at. Rev. Mater. 4 (2019) 515–534, https://doi.org/10.1038/s41578-019-0121-4.
[23] M. Easton, D. StJohn, Grain refinement of aluminum alloys: Part I. the nucleant and solute paradigms-a review of the literature, Metall. Mater. Trans. A 30(6) (1999) 1613-1623, https://doi.org/10.1007/s11661-999-0098-5.
[24] M. Easton, D. StJohn, Grain refinement of aluminum alloys: Part II. Confirmation of, and a mechanism for, the solute paradigm, Metall. Mater. Trans. A 30(6) (1999) 1625-1633,

https://doi.org/10.1007/s11661-999-0099-4.
[25] A.L. Greer, A.M. Bunn, A. Tronche, P.V. Evans, D.J. Bristow, Modelling of inoculation of metallic melts: application to grain refinement of aluminium by Al–Ti–B, Acta Mater. 48(11) (2000) 2823-2835, https://doi.org/10.1016/S1359-6454(00)00094-X.
[26] F. Wang, D. Qiu, Z.-L. Liu, J.A. Taylor, M.A. Easton, M.-X. Zhang, The grain refinement mechanism of cast aluminium by zirconium, Acta Mater. 61(15) (2013) 5636-5645, https://doi.org/10.1016/j.actam at.2013.05.044.
[27] F. Wang, Z. Liu, D. Qiu, J.A. Taylor, M.A. Easton, M.-X. Zhang, Revisiting the role of peritectics in grain refinement of Al alloys, Acta Mater. 61(1) (2013) 360-370, https://doi.org/10.1016/j.actam at.2012.09.075.
[28] W. Kurz, D.J. Fisher, Fundamentals of solidification, Trans Tech Publications1998.
[29] B. Gludovatz, E.P. George, R.O. Ritchie, Processing, Microstructure and Mechanical Properties of the CrMnFeCoNi High-Entropy Alloy, JOM 67(10) (2015) 2262-2270, https://doi.org/10.1007/s11837-015-1589-z.
[30] X.W. Liu, L. Liu, G. Liu, X.X. Wu, D.H. Lu, J.Q. Yao, W.M. Jiang, Z.T. Fan, W.B. Zhang, The role of carbon in grain refinement of cast CrFeCoNi high-entropy alloys, Metall. Mater. Trans. A 49(6) (2018) 2151-2160, https://doi.org/10.1007/s11661-018-4549-8.
[31] X.W. Liu, G. Laplanche, A. Kostka, S.G. Fries, J. Pfetzing-Micklich, G. Liu, E.P. George, Columnar to equiaxed transition and grain refinement of cast CrCoNi medium-entropy alloy by microalloying with titanium and carbon, J. Alloys Compd. 775 (2019) 1068-1076, https://doi.org/10.1016/j.jallcom.2018.10.187.
[32] T.E. Quested, Understanding mechanisms of grain refinement of aluminium alloys by inoculation, Mater. Sci. Technol. 20(11) (2004) 1357-1369, https://doi.org/10.1179/026708304225022359.
[33] T. Campanella, C. Charbon, M. Rappaz, Grain refinement induced by electromagnetic stirring: A dendrite fragmentation criterion, Metall. Mater. Trans. A 35(10) (2004) 3201-3210, https://doi.org/10.1007/s11661-004-0064-1.
[34] R. Günther, C. Hartig, R. Bormann, Grain refinement of AZ31 by (SiC)P: Theoretical calculation and experiment, Acta Mater. 54(20) (2006) 5591-5597, https://doi.org/10.1016/j.actam at.2006.07.035.
[35] E. Liotti, A. Lui, R. Vincent, S. Kumar, Z. Guo, T. Connolley, I.P. Dolbnya, M. Hart, L. Arnberg, R.H. Mathiesen, P.S. Grant, A synchrotron X-ray radiography study of dendrite fragmentation induced by a pulsed electromagnetic field in an Al–15Cu alloy, Acta Mater. 70 (2014) 228-239, https://doi.org/10.1016/j.actam at.2014.02.024.
[36] I. Maxwell, A. Hellawell, A simple model for grain refinement during solidification, Acta Metallurgica 23(2) (1975) 229-237, https://doi.org/10.1016/0001-6160(75)90188-1.
[37] M. Asta, C. Beckermann, A. Karma, W. Kurz, R. Napolitano, M. Plapp, G. Purdy, M. Rappaz, R. Trivedi, Solidification microstructures and solid-state parallels: Recent developments, future directions, Acta Mater. 57(4) (2009) 941-971, https://doi.org/10.1016/j.actam at.2008.10.020.
[38] M. Qian, P. Cao, M.A. Easton, S.D. McDonald, D.H. StJohn, An analytical model for constitutional supercooling-driven grain formation and grain size prediction, Acta Mater. 58(9) (2010) 3262-3270, https://doi.org/10.1016/j.actam at.2010.01.052.
[39] M.A. Easton, M. Qian, A. Prasad, D.H. StJohn, Recent advances in grain refinement of light metals and alloys, Current Opinion in Solid State and Materials Science 20(1) (2015) 13-24,

https://doi.org/10.1016/j.cossms.2015.10.001.
[40] M.X. Zhang, P.M. Kelly, M.A. Easton, J.A. Taylor, Crystallographic study of grain refinement in aluminum alloys using the edge-to-edge matching model, Acta Mater. 53(5) (2005) 1427-1438, https://doi.org/10.1016/j.actam at.2004.11.037.
[41] Y.C. Lee, A.K. Dahle, D.H. StJohn, The role of solute in grain refinement of magnesium, Metall. Mater. Trans. A 31(11) (2000) 2895-2906, https://doi.org/10.1007/BF02830349.
[42] J.A. Spittle, Columnar to equiaxed grain transition in as solidified alloys, Int. Mater. Rev. 51(4) (2006) 247-269, https://doi.org/10.1179/174328006X102493.
[43] L.A. Tarshis, J.L. Walker, J.W. Rutter, Experiments on the solidification structure of alloy castings, Metallurgical Transactions 2(9) (1971) 2589-2597, https://doi.org/10.1007/BF02814899.
[44] J.A. Spittle, S. Sadli, Effect of alloy variables on grain refinement of binary aluminium alloys with Al–Ti–B, Mater. Sci. Technol. 11(6) (1995) 533-537, https://doi.org/10.1179/mst.1995.11.6.533.
[45] M.A. Easton, D.H. StJohn, A model of grain refinement incorporating alloy constitution and potency of heterogeneous nucleant particles, Acta Mater. 49(10) (2001) 1867-1878, https://doi.org/10.1016/S1359-6454(00)00368-2.
[46] T.E. Quested, A.L. Greer, Analytical model linking growth restriction to solute interaction in model Al based ternary systems, Mater. Sci. Technol. 21(9) (2005) 985-994, https://doi.org/10.1179/174328405X51866.
[47] T. Quested, A. Dinsdale, A. Greer, Thermodynamic modelling of growth-restriction effects in aluminium alloys, Acta Mater. 53(5) (2005) 1323-1334, https://doi.org/10.1016/j.actam at.2004.11.024.
[48] P. Schempp, C.E. Cross, A. Pittner, M. Rethmeier, Influence of Solute Content and Solidification Parameters on Grain Refinement of Aluminum Weld Metal, Metall. Mater. Trans. A 44(7) (2013) 3198-3210, https://doi.org/10.1007/s11661-013-1649-3.
[49] Z. Chen, H. Kang, G. Fan, J. Li, Y. Lu, J. Jie, Y. Zhang, T. Li, X. Jian, T. Wang, Grain refinement of hypoeutectic Al-Si alloys with B, Acta Mater. 120 (2016) 168-178, https://doi.org/10.1016/j.actam at.2016.08.045.
[50] G. Chai, L. Bäackerud, L. Arnberg, Relation between grain size and coherency parameters in aluminium alloys, Mater. Sci. Technol. 11(11) (1995) 1099-1103, https://doi.org/10.1179/mst.1995.11.11.1099.
[51] W.H. Liu, Z.P. Lu, J.Y. He, J.H. Luan, Z.J. Wang, B. Liu, Y. Liu, M.W. Chen, C.T. Liu, Ductile CoCrFeNiMox high entropy alloys strengthened by hard intermetallic phases, Acta Mater. 116 (2016) 332-342, http://dx.doi.org/10.1016/j.actam at.2016.06.063.
[52] Y.L. Zhao, T. Yang, Y. Tong, J. Wang, J.H. Luan, Z.B. Jiao, D. Chen, Y. Yang, A. Hu, C.T. Liu, J.J. Kai, Heterogeneous precipitation behavior and stacking-fault-mediated deformation in a CoCrNi-based medium-entropy alloy, Acta Mater. 138 (2017) 72-82, https://doi.org/10.1016/j.actam at.2017.07.029.
[53] B. Sundman, B. Jansson, J.-O. Andersson, The Thermo-Calc databank system, Calphad 9(2) (1985) 153-190, https://doi.org/10.1016/0364-5916(85)90021-5.
[54] Y. Shan, X. Luo, X. Hu, S. Liu, Mechanisms of Solidification Structure Improvement of Ultra Pure 17 wt pct Cr Ferritic Stainless Steel by Ti, Nb Addition, J. Mater. Sci. Technol. 27(4) (2011) 352-358, https://doi.org/10.1016/S1005-0302(11)60073-X.
[55] P. Nash, The Cr−Ni (Chromium-Nickel) system, Bulletin of Alloy Phase Diagrams 7(5) (1986) 466-476, https://doi.org/10.1007/BF02867812.

[56] T. Nishizawa, K. Ishida, The Co−Ni (Cobalt-Nickel) system, Bulletin of Alloy Phase Diagrams 4(4) (1983) 390-395, https://doi.org/10.1007/BF02868090.
[57] L.J. Swartzendruber, V.P. Itkin, C.B. Alcock, The Fe-Ni (iron-nickel) system, Journal of Phase Equilibria 12(3) (1991) 288-312, https://doi.org/10.1007/BF02649918.